# ANALYSIS OF THE APPLICABILITY OF X-BAND AND S-BAND RADAR DATA OVER SEVERE CONVECTIVE REGION IN NORTHERN JIANGSU, CHINA

JIA, W.[1,2] – QIN, M.[3*]

[1]*Weather Modification Centre of Jiangsu Province, No.8, Yushun Rd., Nanjing 210000, China*

[2]*China Meteorological Administration Aerosol-Cloud and Precipitation Key Laboratory, Nanjing University of Information Science and Technology, No.219, Ningliu Rd., Nanjing 210044, China*

[3]*Meteorology Bureau of Yancheng City, No.1, Dongting Rd., Yancheng 224000, China*

[*]*Corresponding author*
*e-mail: meiqin740@163.com*

(Received 15th Mar 2025; accepted 13th May 2025)

**Abstract.** This study investigated the operational applicability of dual-polarization weather radars in observation and analysis of severe weather phenomena over Northern Jiangsu coastal region located in the mid-latitude of China with the flat and open terrain, based on one S-band radar and new-built five X-band radars. The research focused on diverse hazardous events over this region, including the large-scale event of rain-snow-freezing and local-scale events of thunderstorm gales, short-term heavy precipitation, hail, and tornadoes, while systematically evaluating both radar systems' capabilities in observing these events and analysing their formation mechanisms. The results showed that the dual-polarization products of X-band radar were of higher quality, offering more accurate identification of the melting layer, precipitation phase, hail, and rain droplet size. The X-band radar also provided detailed horizontal and vertical structures, including Differential Reflectivity (ZDR) columns linked to intense updrafts, mid-level radial convergence and storm vertical development. When strong echoes of X-band radar were accompanied by ZDR values less than 0.5 and Correlation Coefficient (CC) values below 0.9, hail can be identified. The X-band radar effectively complemented the S-band radar by filling gaps in low-level observation, demonstrating the stronger observation capabilities for low-level weak echoes and the ability to observe lower-altitude features such as echo outflow boundaries, sea breeze fronts, gust fronts, and low-level high wind-speed areas, which hold the indicative information for enhancing the capabilities of severe convective weather early-warning in the region. However, compared to the S-band radar, the X-band radar had limitations, including the shorter detection range and significant echo attenuation. Therefore, in the operational work, both S-band and X-band radars need to be used together, complementing each other. Special attention should be given to the low-elevation reflectivity factor, radial velocity, and dual-polarization products of X-band radar.
**Keywords:** *Northern Jiangsu, large-scale rain-snow-freezing event, detailed horizontal and vertical echo structures, low-level echo features, indicative early-warning information for severe convective weather*

## Introduction

In recent years, due to the global and regional climate change, extreme weather events have occurred frequently, and the losses caused by these events have aggravated with the development of social economy (Hartmann et al., 2013; Nguyen et al., 2018; Papalexiou and Montanari, 2019; Takahashi and Fujinami, 2021; Sun et al., 2021). Severe convective weather may cause tree falls and foliage damage, affecting the stability of forest ecosystems. During dry seasons, lightning can ignite forest fires, leading to large-scale vegetation loss and destruction of wildlife habitats. In mountainous and hilly regions, short-duration heavy rainfall may trigger landslides and debris flows, posing serious threats to the ecological environment and human activities. Intense rainfall can also


http://www.aloki.hu ● ISSN 1589 1623 (Print) ● ISSN 1785 0037 (Online)
DOI: http://dx.doi.org/10.15666/aeer/2304_71997219

exacerbate soil erosion, reducing farmland fertility and impacting agricultural production. Therefore, enhancing the precise observation of severe convective weather and implementing timely protective measures can help mitigate its adverse impact on the ecological environment.

The forecast and early warning of sudden severe weather, mainly rely on the application of radar data. To improve the accuracy and timeliness of forecasts and warnings, high-resolution X-band mobile small radars, capable of detecting precise and detailed observations, have been deployed to supplement the detection gaps in S-band radar coverage, especially in areas prone to disastrous weather (Wu et al., 2014; Ma et al., 2019). Due to differences in the sampling space of the two weather radar systems, path attenuation, radar performance and parameter, and non-periodic calibration, products from the X-band and S-band radars, a comparative analysis of the similarities and differences between X-band and S-band radar data, and an investigation into the causes of these discrepancies, will further reveal the advantages and limitations of X-band radar. This understanding will allow for better utilization of the X-band radar in areas where the S-band radar experiences faults or detection gaps, thus providing an accurate basis for short-term forecasts of important weather events. The joint application of data from different radar bands and the networked observation of weather radar systems are of significant importance.

In recent years, there have been an increasing amount of research on the application of X-band dual-polarization radar. Some cities internationally have used several X-band radars with smaller detection ranges and higher spatiotemporal resolutions to supplement the limitations of operational radar in urban fine-scale precipitation observation (Chen and Chandrasekar, 2015; Cifelli et al., 2018). Some cities and their surrounding areas in China have also deployed X-band radars with high temporal and spatial resolution to meet practical operational needs. Scholars have conducted extensive research on the detection capabilities of X-band radars. For example, Ma et al. (2012) studied the impact of electromagnetic wave attenuation from the X-band dual-polarization radar on hail identification, pointing out that the attenuation of electromagnetic waves in the rain area can lead to inaccurate hail identification. After attenuation correction, the Differential Reflectivity (ZDR) can more effectively identify hail. Wang et al. (2017) found that parameters such as ZDR and Specific Differential Phase (KDP) from the X-band dual-polarization radar can provide more features for hail identification. Li et al. (2017) integrated the parameters of X-band dual-linear polarization weather radar with the environmental temperature data to analyze the distribution and evolution of various hydrometeor particles in thunderstorm cells. Zhang et al. (2018) studied the application of X-band dual-polarization weather radar in hail identification, noting that particle identification using Hydrometeor Classification (HCL) and other parameters from X-band radar could effectively indicate hail. Li et al. (2020) found that parameters like ZDR and Correlation Coefficient (CC) from the X-band dual-polarization radar could effectively improve hail identification. Zhuang et al. (2023) integrated radar quantitative precipitation estimation to apply X-band dual-polarization radar for capturing heavy precipitation cores in mountainous debris-flow-prone areas with sparse rain gauge coverage. Song et al. (2023) demonstrated that X-band dual-polarization radar exhibited superior advantages in hydrometeor classification during severe convective weather events. Zhi et al. (2024) successfully detected the developmental process of a parent mini-supercell associated with tornado genesis and the evolution characteristics of tornado vortex using X-band dual-polarization radar observations. These studies all demonstrated


http://www.aloki.hu ● ISSN 1589 1623 (Print) ● ISSN 1785 0037 (Online)
DOI: http://dx.doi.org/10.15666/aeer/2304_71997219

the positive role of X-band radar in short-term observation and early warning of hazardous weather. However, due to the significant attenuation inherent in X-band radar, many scholars had compared S-band and X-band radar products. For instance, Tian et al. (2021) compared the detection capabilities of S-band and X-band radar during a stratiform precipitation process. Their results showed that the echo intensity and radial velocity were similar in both bands, but the X-band radar could reflect more detailed structural information. Zhang et al. (2021), through comparisons in quantitative precipitation estimation applications, found that the X-band radar performed better in precipitation estimation. Su and Liu (2022) also found that the X-band radar exhibited the superior performance in observing and identifying strong weather echoes compared to the S-band radar, with advantages such as the longer duration, more detailed vertical structure, larger difference in positive and negative velocity, and finer evolution throughout the weather process. Zhang et al. (2023) found that the X-band radar also observed the characteristics of ZDR arc and melting hail in the lower layers similar to the S-band radar, but highlighted the need to account for attenuation effects in applications. Chen et al. (2024) revealed that the detection results of X-band radar for tornado locations, radial velocities, and storm diameters showed good consistency with the S-band radar, with the peak periods of X-band radar echo tops aligning with the occurrence of cloud top upwelling. Current researches on severe weather observation using X-band and S-band radars in China primarily focused on northern regions centered around Beijing and southern areas around Guangzhou, while relatively fewer studies had been conducted in coastal regions centered on Shanghai. Located in the mid-latitudes within a transitional climate zone between northern and southern China, this coastal region experiences more diverse severe weather phenomena. Beyond localized severe convection and hail, it also encounters large-scale rain-snow-freezing disasters. The northern part of this coastal region which is also named as Northern Jiangsu region and characterized by China's flattest and most open terrain, frequently experienced maritime easterly flows that trigger convective disturbances in the lower atmosphere, resulting in more complex and varied severe weather formation mechanisms. In recent years, frequent tornado occurrences had made Northern Jiangsu one of China's most severe convective disaster areas. To meet the demand for refined severe weather observation and early warning, five new X-band radars had been deployed. This study focuses on Northern Jiangsu, investigating various severe weather events including rain-snow-freezing, thunderstorm gales, short-term heavy precipitation, hail, and tornadoes. By integrating data from an existing S-band radar and building upon previous research, we aimed to: 1) Validate and analyze the applicability of X-band and S-band radars under different weather backgrounds in this region; 2) Compare the strengths and limitations of X-band/S-band radar products and their utility in short-term nowcasting; 3) Develop reference indicators for observation and early-warning. The findings provided crucial references for multi-band radar joint observation and early-warning of severe weather in Northern Jiangsu.

## Materials and methods

Over the region of Northern Jiangsu in China, five X-band radar systems are located in Xinghua, Dafeng, Baoying, Funing, and Yandu (*Figure 1*). These five X-band radars have been networked together to provide coverage for the region of Northern Jiangsu. Additionally, there is an S-band radar in Yancheng. The collaboration between X-band


http://www.aloki.hu ● ISSN 1589 1623 (Print) ● ISSN 1785 0037 (Online)
DOI: http://dx.doi.org/10.15666/aeer/2304_71997219

and S-band radars enhances radar detection precision for the region (Zhuang et al., 2023; Zhang et al., 2023; Chen et al., 2024; Zhao et al., 2025).


***Figure 1.*** *The distribution of X-band and S-band radars in Northern Jiangsu*

The X-band and S-band radars mainly provide the products of Reflectivity factor (Z), ZDR, CC, KDP, and radial velocity (V) to observe severe convective weather. The formulation of these products is as follows.

$$Z = \sum D_i^6 \quad \text{(Eq.1)}$$

Z is the Reflectivity factor, which could be used to analyze the type and intensity of precipitation. $D_i$ is diameter of the i-th precipitation particle.

$$ZDR = 10 \times \log\frac{Z_{HH}}{Z_{VV}} \quad \text{(Eq.2)}$$

$ZDR$ is the Differential Reflectivity, which could be used to analyze the type of precipitation. $Z_{HH}$ is the horizontal polarized Reflectivity factor. $Z_{VV}$ is the vertical polarized Reflectivity factor.

$$CC = \frac{|\langle S_{VV}S_{HH}^*\rangle|}{[\langle|S_{HH}|^2\rangle\langle|S_{VV}|^2\rangle]^{0.5}} \quad \text{(Eq.3)}$$

$$S_{HH} = \frac{1}{M}\sum_{i=1}^{M} H_i^* H_i \quad \text{(Eq.4)}$$

$$S_{VV} = \frac{1}{M}\sum_{i=1}^{M} V_i^* V_i \quad \text{(Eq.5)}$$

$CC$ is the Correlation Coefficient, which could be used to analyze the type of precipitation and detect severe convective weather. $S_{HH}$ is the horizontal polarized scattering matrix. $S_{VV}$ is the vetical polarized scattering matrix. $\langle\cdot\rangle$ is the average of different samples. * is the complex conjugate of variables.


http://www.aloki.hu ● ISSN 1589 1623 (Print) ● ISSN 1785 0037 (Online)
DOI: http://dx.doi.org/10.15666/aeer/2304_71997219

$$KDP = \frac{\emptyset_{DP}(r_2)\emptyset_{DP}(r_1)}{2\times(r_2-r_1)} \quad \text{(Eq.6)}$$

$KDP$ is the Specific Differential Phase, which could be used to analyze the intensity of precipitation. $\emptyset_{DP}$ is the Differential Phase Shift. $r_1, r_2$ the location along the radar beam propagation path.

$$V=U_{ew}cos(\theta)cos(\varphi)+V_{sn}sin(\theta)cos(\varphi)+Wsin(\varphi) \quad \text{(Eq.7)}$$

$V$ is the radial velocity, which could be used to detect severe convective weather. $U_{ew}$ is the horizontal wind speed from east to west. $V_{sn}$ is the horizontal wind speed from south to north. $W$ is vertical speed. θ is the azimuth angle of radar**.** Φ is elevation angle of radar. Otherwise, some products such as the Cloud top temperature (TOPS), 1-hour estimated precipitation (OHP), and vertically accumulated liquid water (VIL) could be retrieved from the above main products.

To investigate the applicability of products from X-band and S-band radars under different weather processes, this study selected five types of cases, such as rain-snow-freezing, thunderstorm winds, short-term heavy rainfall, hail, and tornadoes occurrence. For the first type of rain-snow-freezing events, the case from February 20 to 24, 2024 was chosen (Case 1). For the second type of thunderstorm wind events, the case on April 15, 2023 was chosen (Case 2), where wind played a major role. For the third type of short-term heavy rainfall events, the case on August 27, 2023 was chosen (Case 3), where rain was the dominant factor. For the fourth type of hail events, the case on June 10, 2023 was chosen with the appearance of 2–3 cm hail in multiple locations in Yancheng (Case 4). For the fifth type of tornado events, the case of Dafeng tornado on August 13 in 2023 was selected (Case 5).

## Results

### *Application of X-band and S-band radars in hydrometeor phase identification during rain-snow-freezing events*

From February 20 to 24, 2024, Yancheng experienced a persistent rain-snow-freezing weather process. This study investigated the ability of X-band radar to identify different precipitation phases during the event. Based on the formulations of (1), (2), (3), and (6), *Figure 2* compared the detection results of the Yancheng S-band radar and the Xinghua X-band radar at the same height around 18 Coordinated Universal Time (UTC) on February 22. The real-time observation from the automatic stations revealed the presence of graupel in the red-boxed area in the *Figure 2*. Typically, graupel appears similar to hail on dual-polarization radar, but compared to hail, graupel has a much lower Z and a higher CC. The ZDR and KDP values of dry graupel are close to 0. When graupel melts, it is covered by water film, and its ZDR and KDP values approach those of rain. According to the results from the X-band radar, the Z in the red area was between 25 and 40 dBZ, the ZDR was between 0.2 and 2, the KDP was between -0.1 and 1.7, and the CC ranged from 0.7 to 0.99. Compared to the S-band radar, the X-band radar showed a significantly lower and clearer CC for detecting graupel. *Figure 3* compared the detection results of the Yancheng S-band radar and the Dafeng X-band radar at the same height around 18:47 UTC on February 23. Typically, dry snow consists of non-liquid water-encapsulated aggregated snowflakes. Dry snow has a low Z but a high CC. The ZDR of dry snow is


http://www.aloki.hu ● ISSN 1589 1623 (Print) ● ISSN 1785 0037 (Online)
DOI: http://dx.doi.org/10.15666/aeer/2304_71997219

usually between 0 and 0.5 dBZ, but it can be higher when the snowflake aggregation is low. As dry snow begins to melt, the Z, ZDR, and KDP values increase, while the CC decreases. Based on the S-band radar detection, the stronger Z ranged from 20 to 40 dBZ, with ZDR near 0, CC greater than 0.97, and KDP near 0, which aligned with the typical characteristics of snow. When comparing with the X-band detection results, except for the slightly smaller Z, the other parameters were essentially consistent with the S-band radar, but the X-band radar detected at a lower altitude. The X-band radar results were also more refined, as can be seen in the *Figure 3*. Furthermore, *Figure 4* clearly showed that the CC from the X-band radar detected the melting layer height, while the S-band radar product did not, indicating that the X-band radar's polarization product had better observation quality and can more accurately indicate the location of the melting layer.

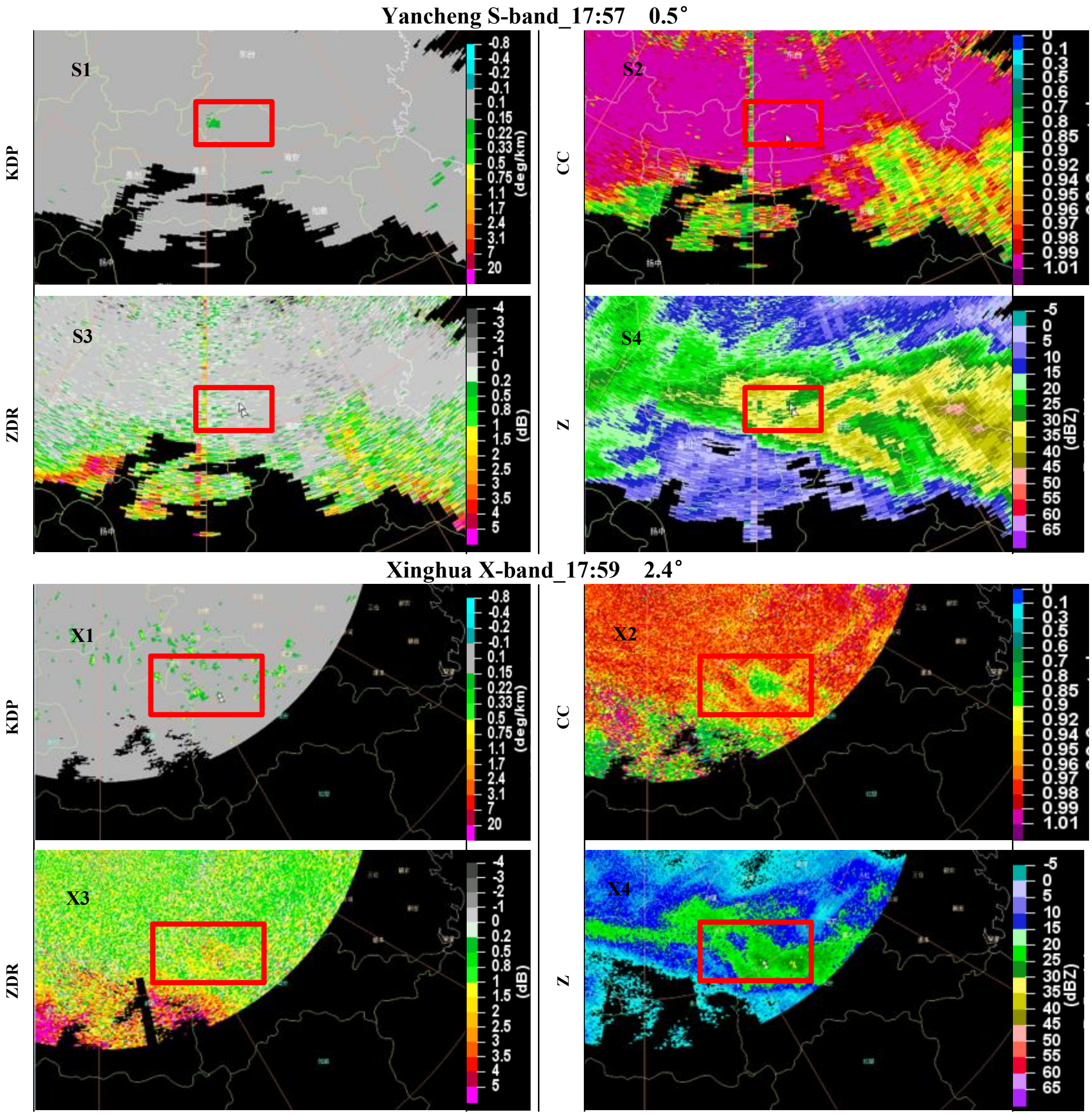


***Figure 2.*** *Specific Differential Phase (KDP), Correlation Coefficient (CC), Differential Reflectivity (ZDR), and Reflectivity factor(Z) at the 1.5° elevation angle of the Yancheng S-band radar at 17:57 UTC (S1,S2,S3,S4) and at the 2.4° elevation angle of the Xinghua X-band radar at 17:59 UTC on February 22, 2024 (X1, X2, X3, X4)*


http://www.aloki.hu ● ISSN 1589 1623 (Print) ● ISSN 1785 0037 (Online)
DOI: http://dx.doi.org/10.15666/aeer/2304_71997219

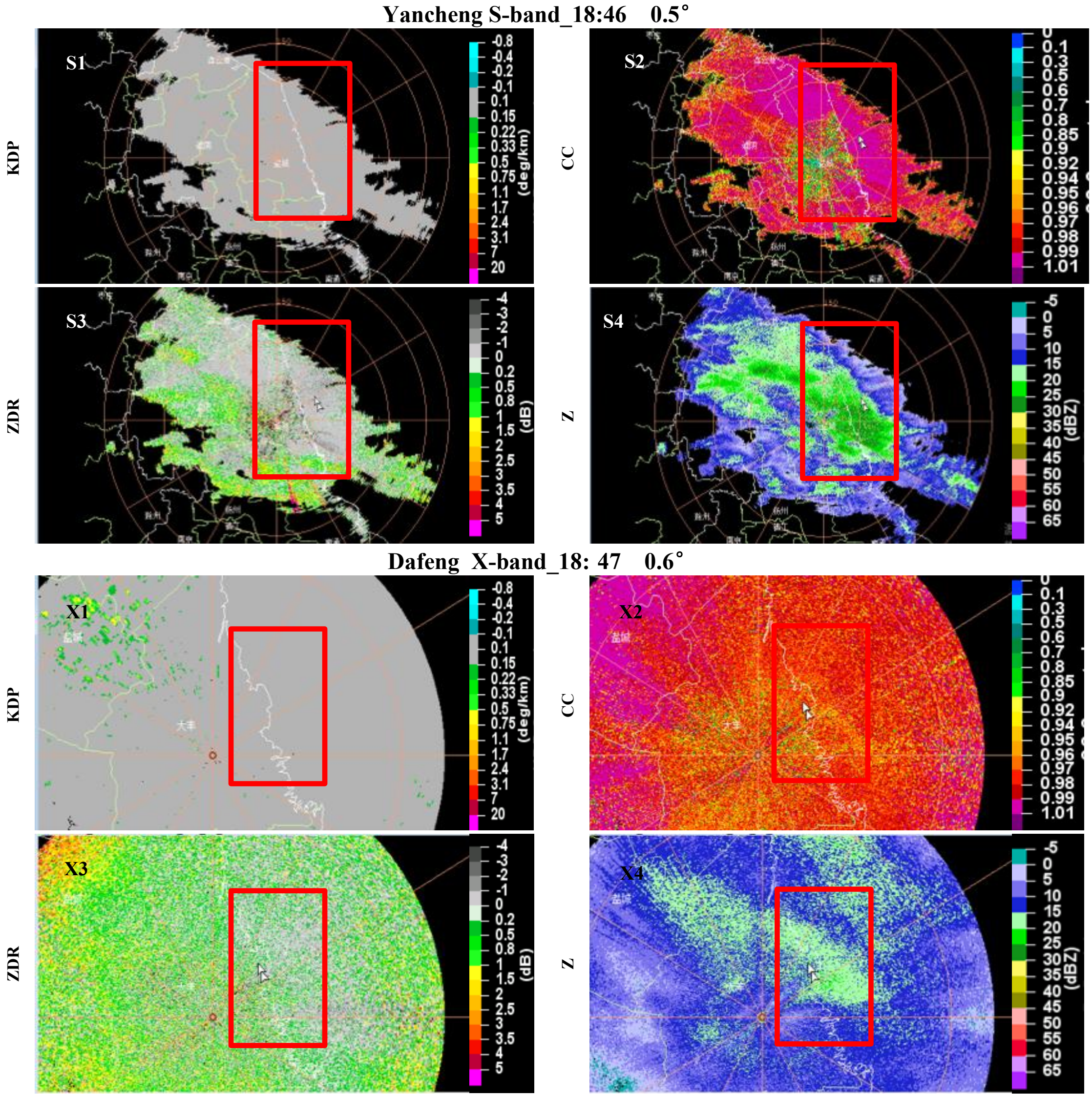


***Figure 3.*** *KDP, CC, ZDR, and Z at the 0.5° elevation angle of the Yancheng S-band radar at 18:46 UTC (S1,S2,S3,S4) and at the 0.6° elevation angle of the Dafeng X-band radar at 18:47 UTC on February 23, 2024 (X1, X2, X3, X4)*

## *Application of X-band and S-band radars in thunderstorm wind events*

On April 15, 2023, Yancheng experienced a wide-area thunderstorm wind event. This event occurred under the background of the Northeast Cold Vortex. At 08:00 UTC, the 500 hPa upper-level temperature trough lagged behind the height trough, with cold advection at high levels. The city was located at the bottom of the cold vortex, with westerly to northwesterly winds prevailing. At 700 hPa, the wind was from the northwest in the trough, and dry cold air continuously intruded. At 850 hPa, the wind was from the northwest at 08:00 UTC, but by 20:00 UTC, it had completely shifted to a southwest wind. As a result, there was the dry cold airflow at high levels and warm moist airflow at low levels, creating unstable stratification conducive to the convection. Additionally, shear lines at both 850 hPa and 925 hPa were located over the northern part of the city, triggering the convection. The strong winds affected most areas of Yancheng, with gusts


http://www.aloki.hu ● ISSN 1589 1623 (Print) ● ISSN 1785 0037 (Online)
DOI: http://dx.doi.org/10.15666/aeer/2304_71997219

exceeding level 9 detected by one-third of the dense automatic stations across the city. From T-lnp diagram at 08:00 UTC on April 15 at Sheyang Station, it was clear that there was a significant intrusion of dry layers from 850 hPa to 500hPa, with high wind speeds at these altitudes. The wind speed at 500 hPa reached 34.4 m/s, and the 0-6 km vertical wind shear reached 34.9 m/s, which was favorable for the storm organization and development. The specific humidity at 850 hPa was 1.21 g/kg, at 700 hPa was 1.18 g/kg, and at 500 hPa was 0.27 g/kg, indicating that the atmosphere was generally dry, which hindered the occurrence of short-term heavy rainfall. As a result, the light to moderate rain occurred throughout the city, with the minimal impact from precipitation.

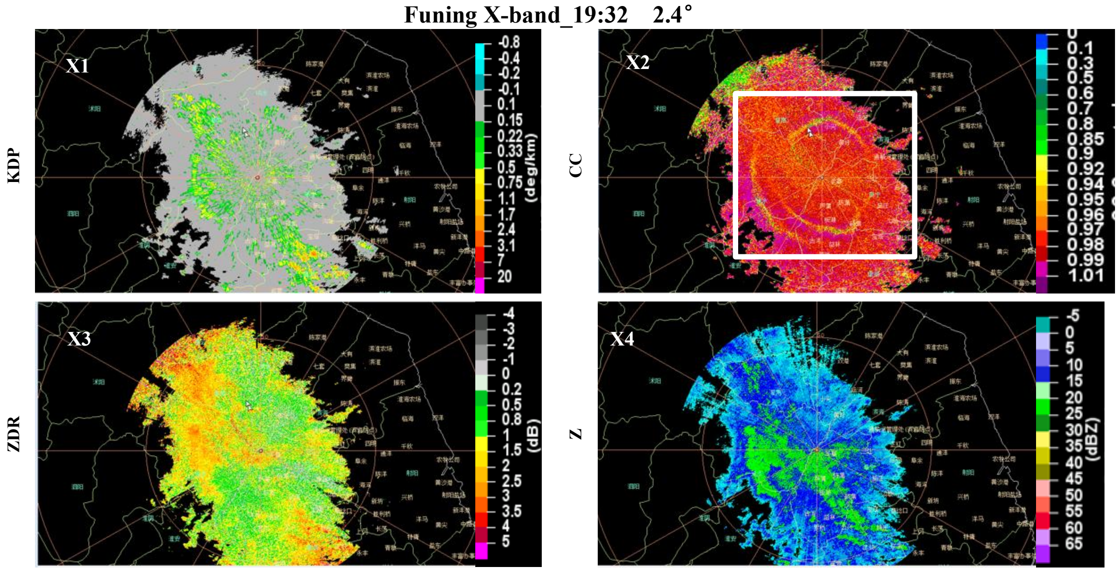


***Figure 4.*** *KDP, CC, ZDR, and Z at the 2.4° elevation angle of the Funing X-band radar at 19:32 UTC on February 23, 2024 (X1, X2, X3, X4)*

Based on the formulations of (1) and (7), *Figure 5* showed the reflectivity factor (Z) and radial velocity (V) at 18:07 UTC on April 15 for the Yancheng S-band radar at a 0.5° elevation angle and at 18:18 UTC for the Funing X-band radar at a 3.3° elevation angle. The heights of the strong echoes detected by both radars were approximately 0.7 km, making the results comparable. From the S-band radar results, it was clear that the bow echo rapidly swept from northwest to southeast, with the strongest echo around 55 dBZ. Areas passed by the bow echo experienced strong winds. From the radial velocity diagram, the S-band radar at its lowest elevation angle did not detect any significant wind regions, with the maximum radial velocity around 15 m/s. In contrast, the X-band radar at Funing showed significant attenuation in the reflectivity factor, with the strongest reflectivity factor around 40 dBZ, but the radial velocity diagram was much more detailed, showing the extent of the strong wind velocity area. The maximum radial velocity reached 27 m/s, and the X-band radar could detect winds at lower altitudes. The 0.6° elevation angle allowed detection of strong wind speed areas at lower heights, providing a reference for observation and early warning in practical applications. *Figure 6* selected the reflectivity factor and radial velocity at 19:55 UTC for the Yancheng S-band radar at a 0.5° elevation angle and the Dafeng X-band radar at a 2.4° elevation angle. From the S-band radar, it can be seen that the bow echo had moved to


http://www.aloki.hu ● ISSN 1589 1623 (Print) ● ISSN 1785 0037 (Online)
DOI: http://dx.doi.org/10.15666/aeer/2304_71997219

the southern part of Yancheng, and compared to the previous time, the bow echo had weakened. The S-band radar was able to reflect the overall shape of the echo well, and at this time, the low elevation angle of 0.5° detected the strong wind speed area, which was quite similar to the X-band radar's velocity diagram. However, due to the limited detection range of the X-band radar at this time, the bow echo could not be clearly seen. Only a part of the fragmented bow echo was detectable. Nonetheless, the details reflected by the X-band radar were more refined. In this specific case, the S-band and X-band radar each had their strengths and weaknesses. The S-band radar suffered the less attenuation of strong convective echoes and provided the better overall shape detection, while the X-band radar experienced the significant attenuation but detected the high wind speed areas, especially low-level strong wind areas, more precisely. In operational work, it was necessary to combine the products of both the X-band and S-band radars for complementary use, which provided better results.

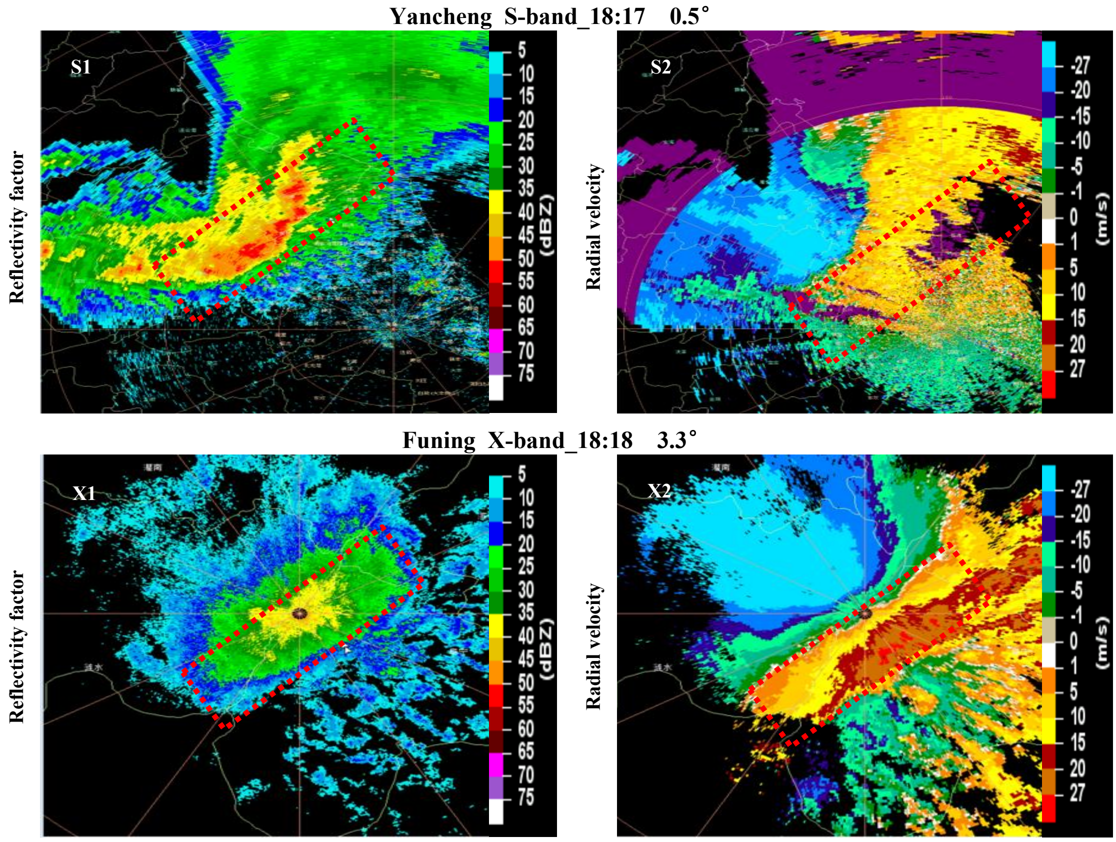


***Figure 5.*** *Reflectivity factor(R) and radial velocity(V) at the 0.5° elevation angle of the Yancheng S-band radar at 18:17 UTC (S1, S2) and at the 3.3° elevation angle of the Funing X-band radar at 18:18 UTC on April 15, 2023 (X1, X2)*

### *Application of X-band and S-band radars in intense precipitation events*

On August 27, 2023, Yancheng experienced the heavy to very heavy rainfall. This event was influenced by an upper-level trough and a surface cyclone. On the 27th, at 500hPa, the city was under the control of southwest airflow ahead of the upper-level trough. At 700 hPa and 850 hPa, low vortex shear moved eastward, and the southwest jet stream south of the shear line provided abundant moisture, favorable for the heavy


http://www.aloki.hu ● ISSN 1589 1623 (Print) ● ISSN 1785 0037 (Online)
DOI: http://dx.doi.org/10.15666/aeer/2304_71997219

rainfall. From the surface pressure field, the Jianghuai cyclone moved northeast, and by 08:00 UTC on the 28th, it entered the sea along the northern coastal area of the city. At 08:00 UTC, the sounding at Sheyang Station showed a deep moist layer, with a specific humidity at 850 hPa near 12 g/kg, a low lifting condensation height, and a K-index reaching 32°C, which favored the heavy rainfall and short-term intense precipitation. The 0-6 km vertical wind shear reached 16 m/s, indicating some instability and a potential for thunderstorms and strong winds. During this event, the heavy to very heavy rainfall occurred across the entire city of Yancheng, accompanied by the short-term intense precipitation (with the maximum hourly rainfall intensity of 109.4 mm/h, recorded in Taipingqiao Village, Gongxing Community, Funing County) and thunderstorms with strong winds. The impact of rainfall was greater than that of the wind during this event.

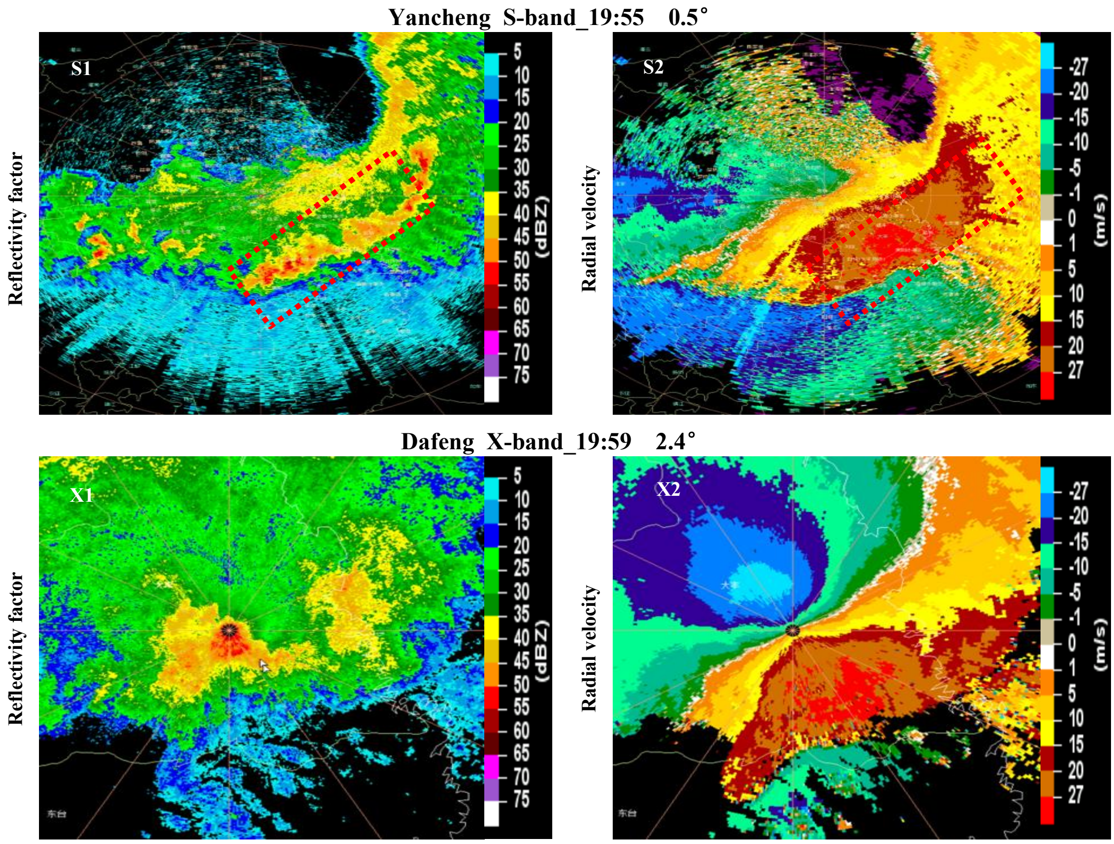


***Figure 6.*** *Reflectivity factor and radial velocity at the 0.5° elevation angle of the Yancheng S-band radar at 19:55 UTC (S1, S2) and at the 2.4° elevation angle of the Dafeng X-band radar at 19:59 UTC on April 15, 2023 (X1, X2)*

*Figures 7 and 8* showed a comparison of various products from the S-band and X-band radars in Funing and Dafeng during this event. *Figure 7* selected the 0.5° elevation angle from the Yancheng S-band radar at 21:18 UTC on August 27 and the 2.4° elevation angle from the Funing X-band radar at 21:18 UTC, comparing TOPS, OHP, VIL, ZDR, V, and Z. From the S-band reflectivity factor, the range of this strong convection was large, with the strong echoes, and the reflectivity at 0.5° elevation reached 50–60 dBZ. The strong echoes were at low altitudes, indicating that strong echoes were near the


http://www.aloki.hu ● ISSN 1589 1623 (Print) ● ISSN 1785 0037 (Online)
DOI: http://dx.doi.org/10.15666/aeer/2304_71997219

surface, which was favorable for the short-term heavy rainfall. The ZDR showed values of 1–2 dB, indicating large raindrops.

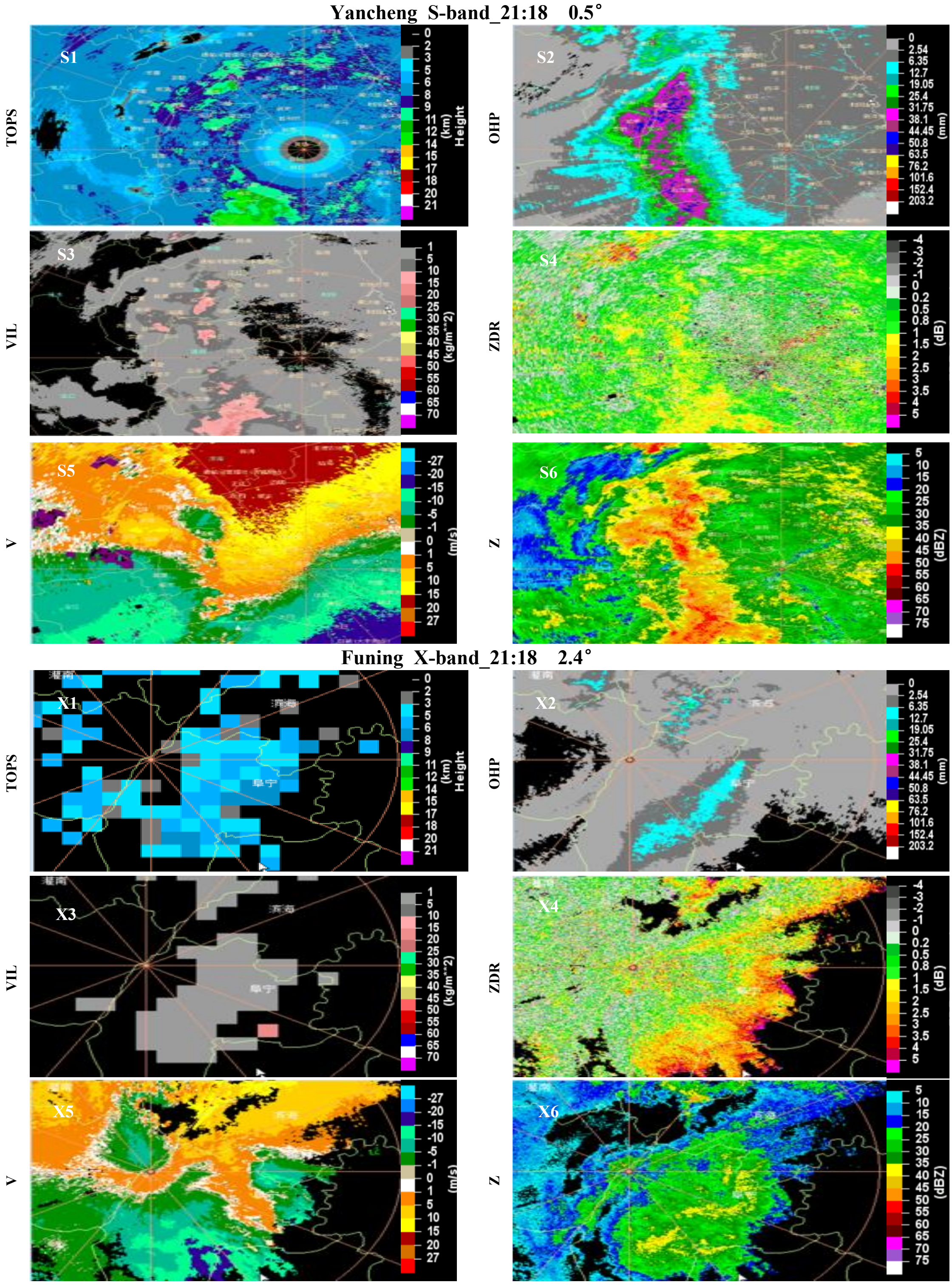


***Figure 7.*** *Cloud top temperature (TOPS), 1-hour estimated precipitation (OHP), vertically accumulated liquid water (VIL), ZDR, V, and Z at the 0.5° elevation angle of the Yancheng S-band radar at 21:18 UTC (S1, S2, S3, S4, S5, S6) and at the 2.4° elevation angle of the Funing X-band radar at 21:18 UTC on August 27, 2023 (X1, X2, X3, X4, X5, X6)*


http://www.aloki.hu ● ISSN 1589 1623 (Print) ● ISSN 1785 0037 (Online)
DOI: http://dx.doi.org/10.15666/aeer/2304_71997219

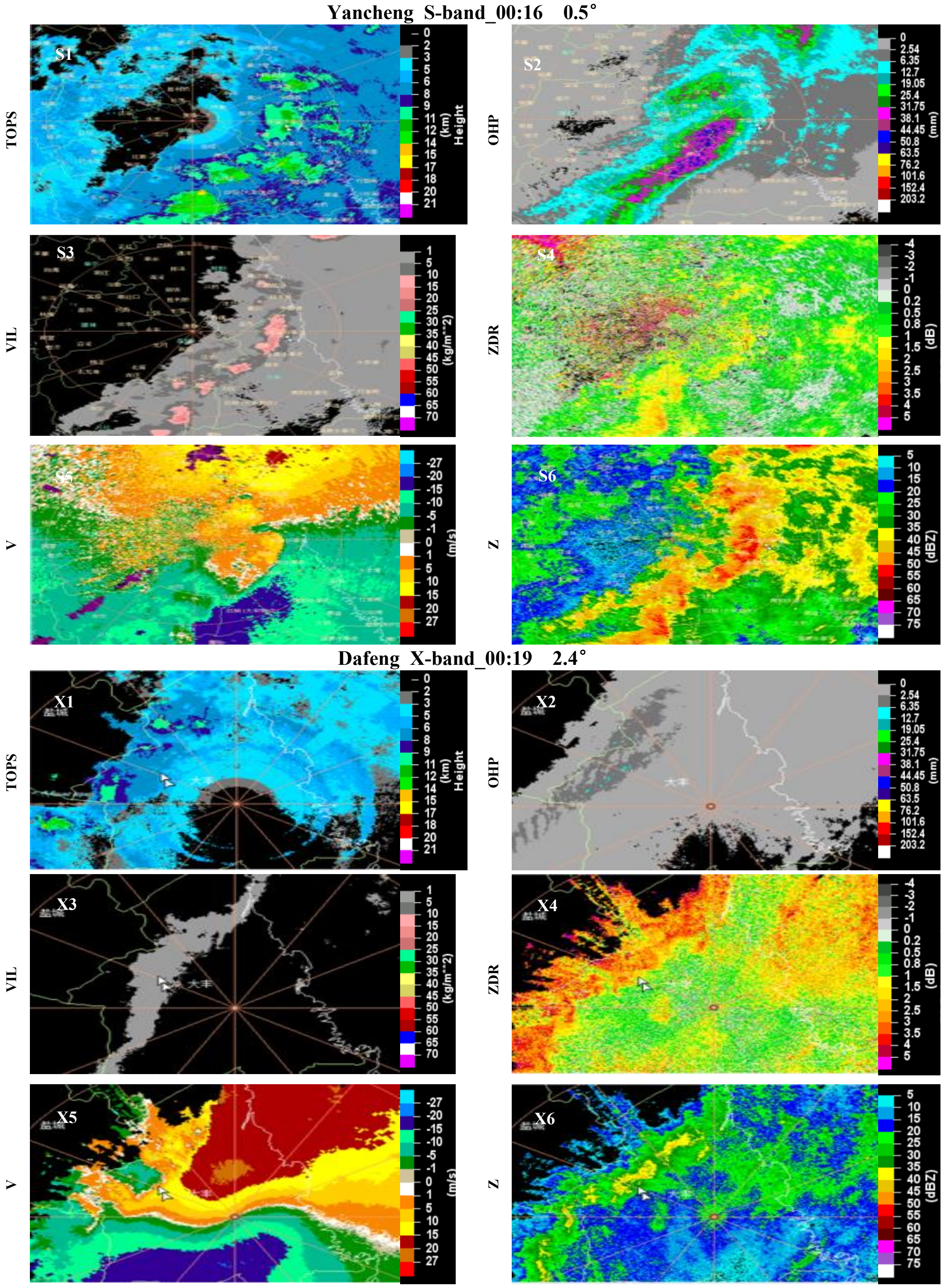


***Figure 8.*** *TOPS, OHP, VIL, ZDR, V, and Z at the 0.5° elevation angle of the Yancheng S-band radar at 00:16 UTC (S1, S2, S3, S4, S5, S6) and at the 2.4° elevation angle of the Dafeng X-band radar at 00:19 UTC on August 27, 2023 (X1, X2, X3, X4, X5, X6)*


http://www.aloki.hu ● ISSN 1589 1623 (Print) ● ISSN 1785 0037 (Online)
DOI: http://dx.doi.org/10.15666/aeer/2304_71997219

However, the cloud top height was not very high, around 11–14 km, and the VIL was between 20–25 kg/m², indicating that the storm was not highly developed and the convection was less organized, without hail. The 1-hour estimated precipitation was between 50-60 mm, slightly lower than the actual observation, but still relatively closed. The radial velocity diagram showed both positive and negative velocities corresponding to the strong echo. Overall, the S-band detection was quite accurate, and the 1-hour accumulated precipitation estimation was reliable. In contrast, the Funing X-band radar showed significant attenuation in the reflectivity factor, with values around 35–40 dBZ for the strong echo. The 1-hour estimated precipitation was only around 5 mm, which was severely underestimated. The VIL was between 1-5 kg/m², and the cloud top height was around 5 km, showing significant attenuation. However, the radial velocity diagram was much clearer and more detailed than the S-band radar, still showing positive and negative velocities. Similarly, *Figure 8* compared the 0.5° elevation angle from the Yancheng S-band radar at 00:16 UTC on August 28 and the 2.4° elevation angle from the Dafeng X-band radar at 00:19 UTC. From the S-band detection, the strongest reflectivity factor was between 55–65 dBZ, and the differential reflectivity was between 1–2 dB, indicating the short-term heavy rainfall. The vertically accumulated liquid water was between 25–30 kg/m², and the cloud top height was 11-14 km, which was similar to the previous situation in Funing, but with slightly enhanced intensity, still dominated by the short-term heavy rainfall. However, the Dafeng X-band radar showed similar severe attenuation, with the reflectivity factor between 30-35 dBZ for the strong echo, vertically accumulated liquid water between 1–5 kg/m², and cloud top height below 5 km. The 1-hour estimated precipitation was about 5 mm, which provided the limited reference value. In conclusion, for processes dominated by the heavy rainfall, X-band radar experienced significant attenuation, and the detection of cloud top height, 1-hour accumulated precipitation, and vertically accumulated liquid water showed considerable errors, making the reference value limited. However, the X-band radar still had advantages in detecting radial velocity. The S-band radar, with the less attenuation of strong echoes, provided more reliable product values, especially in 1-hour estimated precipitation, which can be valuable in operational applications.

### *Application of X-band and S-band radars in hail events*

From 10:00 to 20:00 UTC on June 10, 2023, Yancheng experienced the thunderstorm weather, accompanied by the land winds of 8–9 levels, sea winds of 9–11 levels, and localized hail. Among the dense automatic stations, 19 stations recorded gusts above level 8, with 4 stations reaching level 9 and 1 station reaching level 11 (10 km northeast of Chenjiagang Town, Xiangshui, with a wind speed of 31.7 m/s). The maximum precipitation was 28.3 mm, recorded in the Huan Kecheng area of Tinghu District. Additionally, hail with a diameter of 2–3 cm was observed in Funing County, Sheyang County, Tinghu District, the Economic Development Zone, and Dafeng District.

This strong convective process was also triggered by the continuous formation of gust fronts, so let's first compare the detection of gust fronts by the S-band and X-band radars. *Figure 9* showed the reflectivity factor and radial velocity from the Yancheng S-band radar at 9:52 UTC with a 0.5° elevation angle and the Funing X-band radar at 9:50 UTC with a 0.6° elevation angle. Due to the lower detection altitude of the X-band radar, it had certain advantages. From the reflectivity factor, both radars detected a narrow, weak echo band moving from north to south, identifying the gust front. From the radial velocity diagram, the X-band radar identified the outflow boundary, while the S-band radar did


http://www.aloki.hu ● ISSN 1589 1623 (Print) ● ISSN 1785 0037 (Online)
DOI: http://dx.doi.org/10.15666/aeer/2304_71997219

not. The X-band radar demonstrated the stronger detection capability for weak low-level echoes.

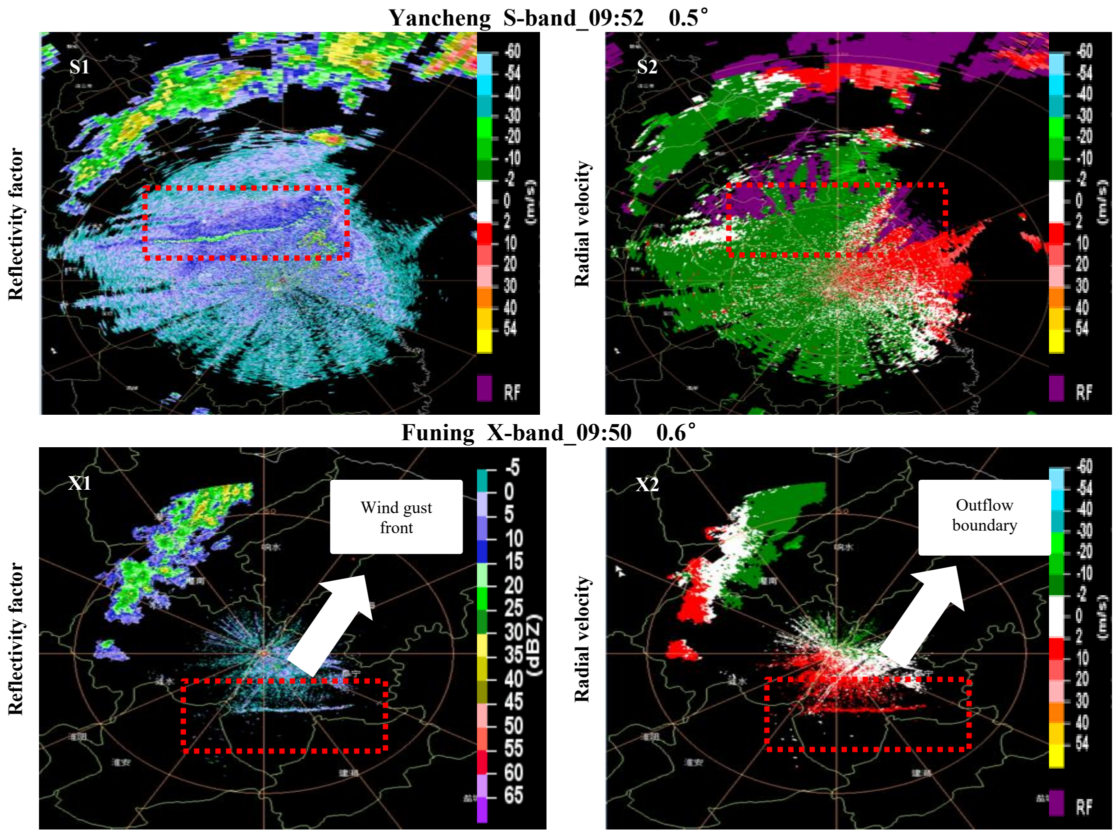


***Figure 9.*** *Reflectivity factor and radial velocity at the 0.5° elevation angle of the Yancheng S-band radar at 09:52 UTC (S1, S2) and at the 0.6° elevation angle of the Funing X-band radar at 09:50 UTC on June 10, 2023 (X1, X2)*

Dual-polarization radar has a clear advantage over conventional radar in the identification of precipitation particles. In short-range forecasting, combining the reflectivity factor with the polarimetric quantities can help classify convective weather types, making it a powerful tool for observation and forecasting severe weather events such as hail and heavy rainfall. Therefore, *Figures 10 and 11* compared the hail detection capability of dual-polarization products from the S-band and X-band radars. *Figure 10* showed the reflectivity factor, vertically accumulated liquid water, differential reflectivity, and correlation coefficient from the Yancheng S-band radar at 16:00 UTC with a 0.5° elevation angle. The large boxes in the *Figure 10* corresponded to the same echo region shown in *Figure 11*. The small box indicated that hail was detected in this area, with the reflectivity factor reaching 60–65 dBZ, vertically accumulated liquid water at 65 kg/m², and a correlation coefficient around 0.85. The differential reflectivity was less than 0.5, consistent with the dual-polarization characteristics of hail. In comparison, the S-band radar showed the significant attenuation of the reflectivity factor, with the strong echo at 45–50 dBZ and vertically accumulated liquid water between 20–25 kg/m², which was notably lower. Although the intensity of the echo had decreased, the observed echo structure was more refined, and the small-scale features were more pronounced.


http://www.aloki.hu ● ISSN 1589 1623 (Print) ● ISSN 1785 0037 (Online)
DOI: http://dx.doi.org/10.15666/aeer/2304_71997219

Additionally, the X-band dual-polarization product also detected the hail characteristics, with the dual-polarization products being more detailed. Thus, in hail detection, the differential reflectivity factor and correlation coefficient of the X-band dual-polarization radar were two important polarimetric quantities. Generally, the differential reflectivity of hail was small, close to 0, and sometimes negative, while the correlation coefficient was typically less than 0.9.

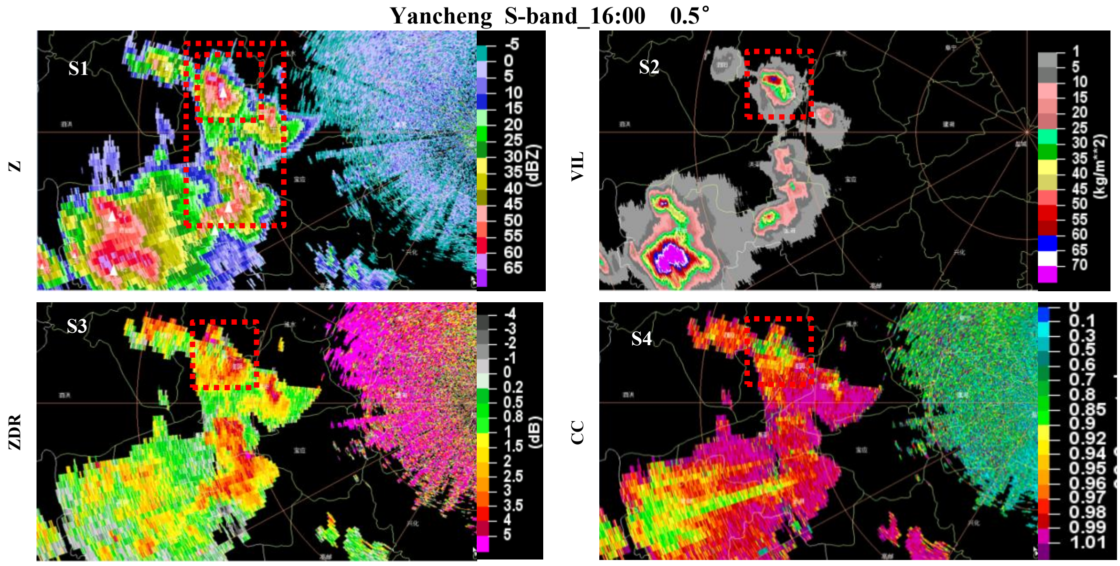


***Figure 10.*** *Z, VIL, ZDR and CC at the 0.5° elevation angle of the Yancheng S-band radar at 16:00 UTC on June 10, 2023 (S1, S2, S3, S4)*

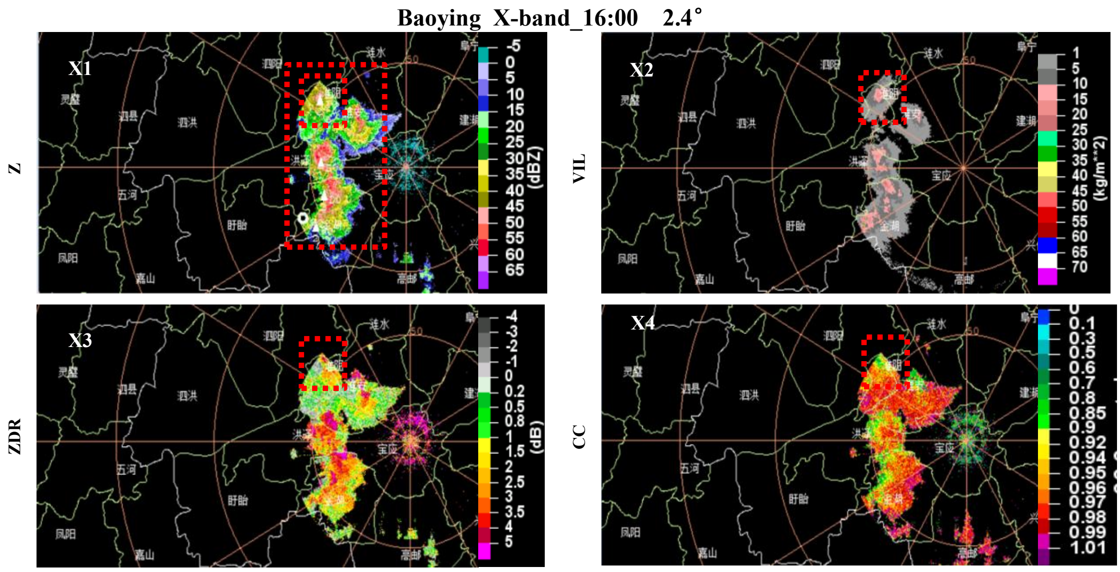


***Figure 11.*** *Z, VIL, ZDR and CC and at the 2.4° elevation angle of the Baoying X-band radar at 16:00 UTC on June 10, 2023 (X1, X2, X3, X4)*


http://www.aloki.hu ● ISSN 1589 1623 (Print) ● ISSN 1785 0037 (Online)
DOI: http://dx.doi.org/10.15666/aeer/2304_71997219

### *Application of X-band and S-band radars in tornado events*

Affected by the upper-level trough and lower-level shear lines, from 11 UTC on August 13, 2023, a strong wind and rain event occurred from north to south across the central and southern parts of Yancheng, accompanied by lightning, short-term heavy rainfall, thunderstorm winds of 8–11 levels, and localized tornadoes. Between 16:00 and 16:15 UTC, the towns of Nanyang, Wanying, Xiaohai, and Caoyan in Dafeng were successively hit by Enhanced Fujita 2 (EF2)-strength tornadoes, which moved in a jump-like pattern. During this event, the 500 hPa upper-level trough moved eastward, with the subtropical high over the sea, and a shear line existed at lower levels. A low vortex formed and developed upstream, moving southeastward, and by 08:00 UTC, it was located in the Huaihe River Basin, moving southeastward, and by 20:00 UTC, it had moved to the Jianghuai area. At 925 hPa, there was a warm center in the southern part of Jiangsu, and by 20:00 UTC, there was a low-pressure center at the surface near this region. When the tornado occurred, influenced by the upper-level trough, the lower levels had shear lines and were in a relatively warm environment, with a surface low-pressure center assisting the process. From the T-lnP diagrams at 08:00 and 20:00 UTC, it can be observed that the lifting condensation level during this process was relatively low, between 970 and 1000 meters, with the small vertical wind shear at the 0–1 km level. The Convective Available Potential Energy(CAPE) value was strong, but this was not a typical environment conducive to tornado formation. Meanwhile, the middle levels were relatively dry, and the lower levels had some moisture, which was more favorable for thunderstorms, strong winds, or downbursts.

*Figure 12* showed the reflectivity factor and radial velocity from the Yancheng S-band radar at 15:55 UTC on the 13th, with a 0.5° elevation angle. From the S-band radar products, a slight hook echo can be observed, and on the velocity diagram, positive and negative velocity pairs appeared consecutively in two scans at 15:55 and 16:01 UTC. This tornado event was a non-supercell tornado, with no mesoscale cyclone warning prior to the tornado, and the Tornado Vortex Signature (TVS) appeared only in one scan, consistent with the actual location, with no advance warning. During this event, the X-band radar in Dafeng was too close to the echo, causing significant attenuation. Therefore, the X-band data from Xinghua and Yandu were selected for analysis.

*Figure 13* showed the reflectivity factor from the Yandu X-band radar at 15:41 UTC with a 0.3° elevation angle, along with the reflectivity factor, radial velocity, and differential reflectivity factor from the 15:51 UTC Range Height Indicator (RHI) scan. It was evident from the *Figure 13* that the echo showed significant attenuation, and the tornado occurred at the edge of the radar's effective range. From the RHI scan results, the storm developed to a high altitude, reaching about 15 km. The radial velocity RHI scan showed the mid-level radial convergence and low-level divergence, accompanied by a ZDR column, indicating the strong updrafts in a high-energy environment. *Figure 14* showed the reflectivity factor from the Xinghua X-band radar at 14:47 and 15:36 UTC with a 0.3° elevation angle, as well as the reflectivity factor and radial velocity from the 15:50 UTC RHI scan. From the *Figure 14*, it was clear that this event was triggered by a sea breeze front, with a distinct structure and clear characteristics. The S-band radar, due to its detection altitude limitation, did not detect this phenomenon. From the reflectivity factor, it can be seen that the precipitation echoes were severely attenuated, with the strongest echo around 40 dBZ. The RHI scan showed that the storm rapidly developed, with strong updrafts and a bounded weak echo region, exhibiting fine vertical structural features.


http://www.aloki.hu ● ISSN 1589 1623 (Print) ● ISSN 1785 0037 (Online)
DOI: http://dx.doi.org/10.15666/aeer/2304_71997219

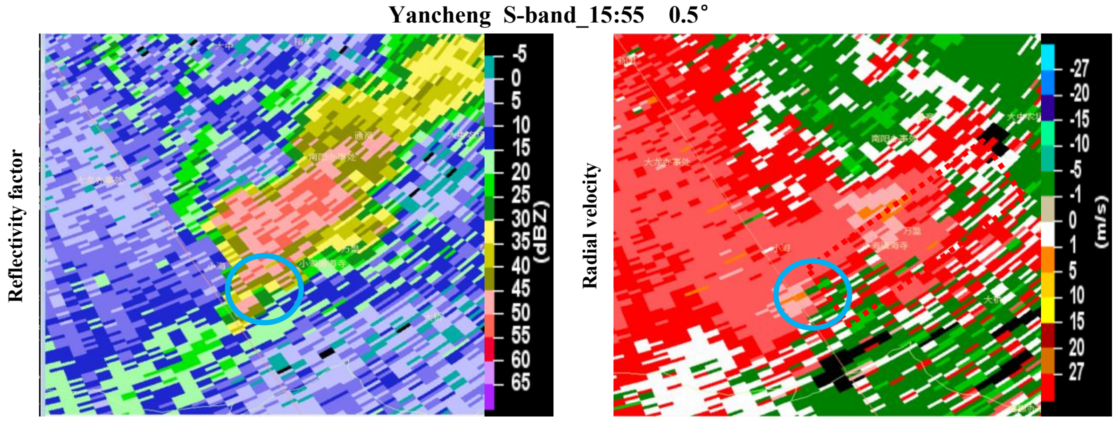


***Figure 12.*** *Reflectivity factor (left) and radial velocity (right) at the 0.5° elevation angle of the Yancheng S-band radar at 15:55 UTC on August 13, 2023*

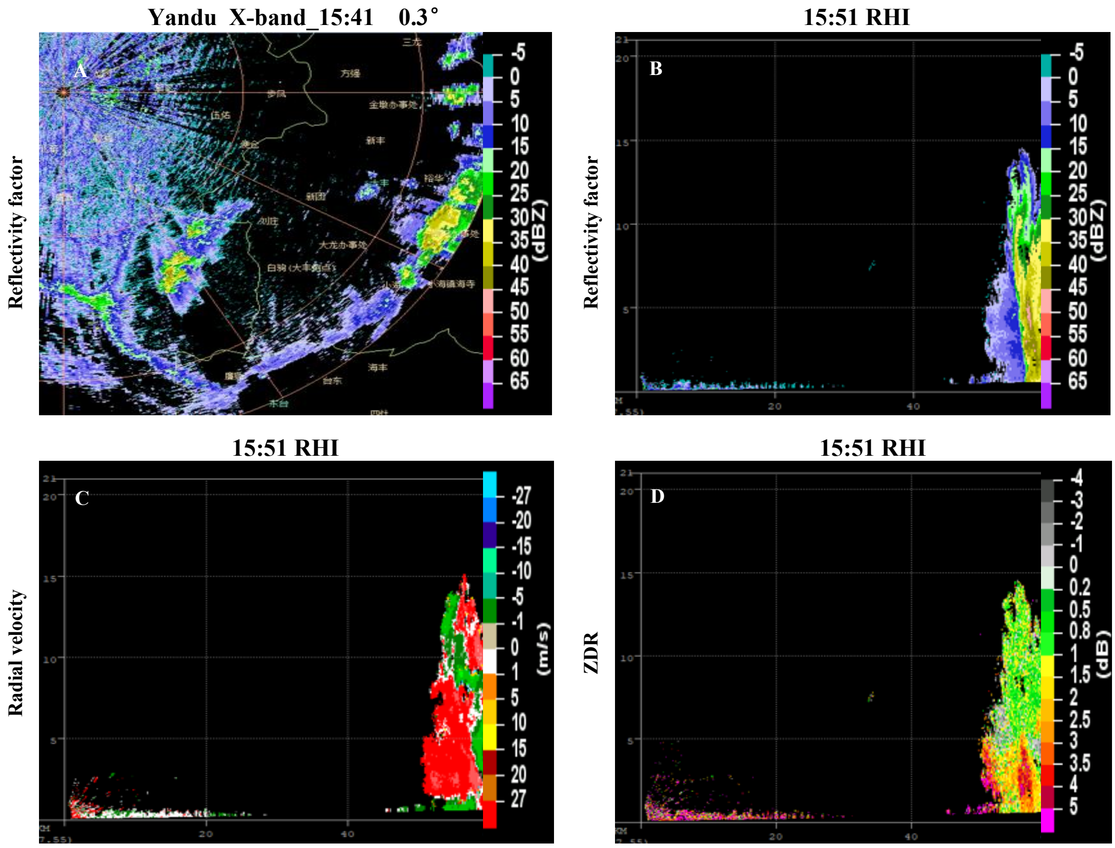


***Figure 13.*** *Reflectivity factor at the 0.3° elevation angle of the Yandu X-band radar at 15:41 UTC (A), and Reflectivity factor (B), radial velocity (C), and ZDR (D) from the Range Height Indicator (RHI) scan at 15:51 UTC on August 13, 2023*


http://www.aloki.hu ● ISSN 1589 1623 (Print) ● ISSN 1785 0037 (Online)
DOI: http://dx.doi.org/10.15666/aeer/2304_71997219

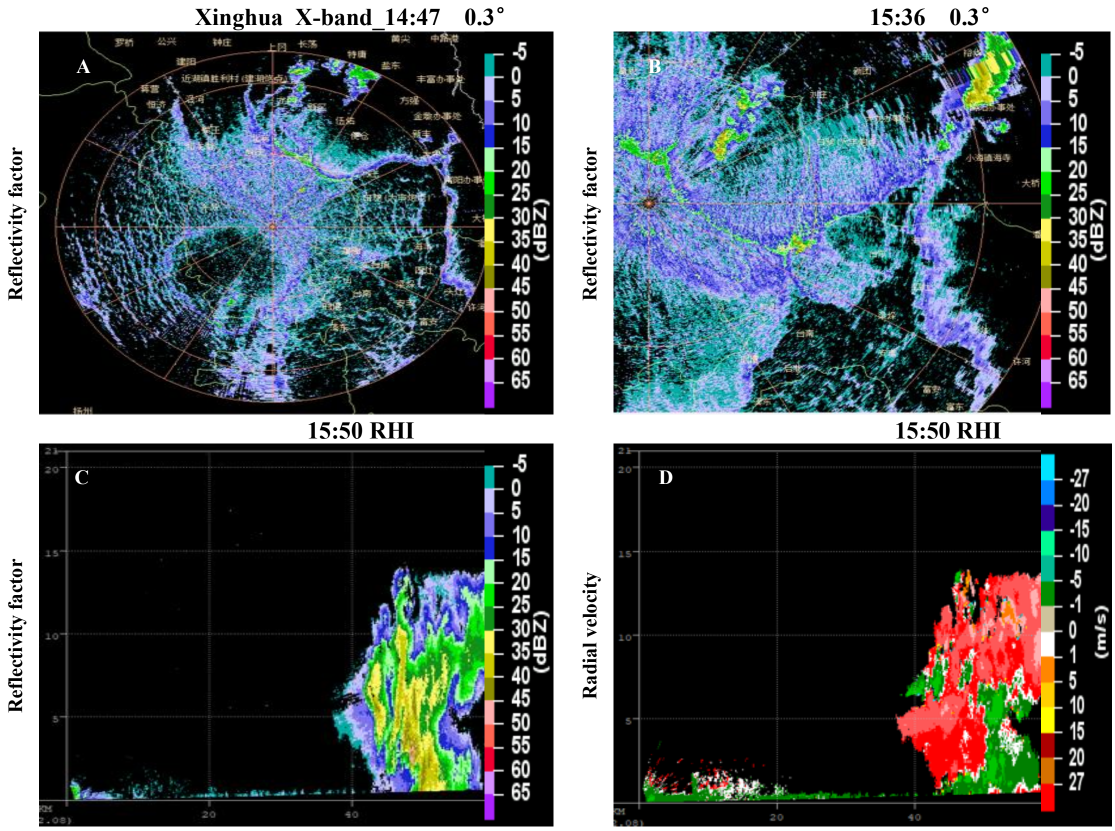


***Figure 14.*** *Reflectivity factor at the 0.3° elevation angle of the Xinghua X-band radar at 14:47 (A) and 15:36 (B) UTC, and reflectivity factor (C) and radial velocity (D) from the RHI scan at 15:50 UTC on August 13, 2023*

## Discussion and conclusions

This study utilized one S-band radar and five new-deployed X-band radars to investigate the disaster-prone Northern Jiangsu region. Given the diversity of severe weather events and the complexity of their formation mechanisms in this area, we analyzed representative cases from recent years including rain-snow-freezing, thunderstorm gales, short-term heavy precipitation, hail, and tornado events. The research specifically examined the operational utility of S-band and X-band radars under different weather backgrounds. Through evaluation of the strengths and limitations of both radar systems' products, we assessed their utility in short-term nowcasting. The findings aimed to establish indicative information for multi-band dual-polarization radar-based early-warning of severe weather phenomena in this region. The specific conclusions were as follows:

(1) For different precipitation phases during large-scale rain-snow-freezing weather events, although X-band radar products were more significantly affected by the reflectivity attenuation, their dual-polarization measurements still performed well. Compared to S-band radars, certain polarimetric variables (such as the correlation coefficient) exhibited the higher observation quality, allowing more accurate phase identification and providing better indications of the melting layer's location.

(2) For heavy precipitation, the shorter wavelength of X-band radar resulted in significant electromagnetic attenuation as the radar beam passed through heavy


http://www.aloki.hu ● ISSN 1589 1623 (Print) ● ISSN 1785 0037 (Online)
DOI: http://dx.doi.org/10.15666/aeer/2304_71997219

precipitation areas. This caused the weaker reflectivity from intense precipitation echoes, leading to larger errors in radar-derived products such as VIL, TOPS, and OHP, and introduced substantial underestimation in precipitation intensity assessments. This can severely impact the forecasters' ability to judge the precipitation intensity and duration. However, high values of ZDR and KDP can still effectively indicate heavy rainfall. Furthermore, the X-band radar's dual-polarization products demonstrated better performance in detecting heavy precipitation than the S-band radar. For thunderstorm gales, X-band radar demonstrated superior precision in radial velocity measurements, particularly excelling in detecting high-velocity zones at lower atmospheric levels. Its enhanced detection capability for weak low-altitude echoes maked it especially valuable in observation of weak low-altitude echoes.

(3) During severe weather events such as hail, X-band dual-polarization products can also detect hail characteristics with greater detail and clarity, making them easier to identify. Two key polarimetric variables of X-band dual-polarization radar were ZDR and CC. When strong echoes were accompanied by ZDR values less than 0.5 (sometimes negative) and CC values below 0.9, hail can be identified. However, due to the attenuation, the reflectivity factor and vertically integrated liquid water observed by the X-band radar were generally lower than those observed by the S-band radar, making their thresholds for identifying hail correspondingly lower. Additionally, X-band radar demonstrated clearer identification of high-wind zones, enhancing the observation capabilities of thunderstorm gale. Its lower detection altitude and superior weak echo detection capacity at low levels enabled precise observation of convective triggers such as gust fronts, providing critical lead time for severe weather early-warning. Although subject to signal attenuation effects, X-band radar achieved higher-resolution storm structure visualization with more distinct small-scale features.

(4) During tornadic supercell events, X-band radar maintained consistent tornado detection criteria with S-band systems, primarily through structural analysis of severe storm features such as updraft-associated ZDR columns. However, X-band demonstrated superior resolution in storm structure observation compared to S-band radar, with the latter showing partial detail loss in S-band radar observations. Specifically, X-band radar achieved finer detection of critical storm characteristics including hook echoes and bounded weak echo regions. Its RHI scanning enabled detailed vertical cross-sectional analysis, such as the characteristics of storm vertical development heights, mid-level radial convergence, and ZDR column. The enhanced low-level detection capability enabled earlier identification of marine breeze front-triggered convective initiation mechanisms at lower altitudes, providing critical lead time for severe weather early-warning.

In summary, while X-band radar exhibited limitations compared to S-band systems in terms of shorter detection range and more severe signal attenuation requiring networked collaborative observation, it offered distinct advantages: 1) X-band radar exhibited superior dual-polarization product quality in precipitation phase identification, particularly excelling in melting layer detection during large-scale snow-ice events, hydrometeor classification, and localized hail recognition; 2) Its enhanced resolution enabled detailed observation of storm structures, including ZDR columns linked to intense updrafts, mid-level radial convergence and storm vertical development; 3) Critically, X-band radar addressed S-band's limitations in low-level observation by detecting weak low-altitude echoes with higher sensitivity, such as observations of outflow boundaries, sea breeze fronts, and gust fronts and high-velocity zones at lower


http://www.aloki.hu ● ISSN 1589 1623 (Print) ● ISSN 1785 0037 (Online)
DOI: http://dx.doi.org/10.15666/aeer/2304_71997219

atmosphere. These capabilities proved valuable for the early-warning of severe weather under various backgrounds with different formation mechanisms in Northern Jiangsu region—a flat and coastal area. Therefore, operational implementation required synergistic use of both bands, with X-band data emphasizing lower-elevation reflectivity, radial velocity, and dual-polarization products. The above findings provided critical guidance for optimizing multi-band radar applications in disaster observation over Northern Jiangsu region. The enhanced early-warning capacity carried significant socioeconomic value for this economically vibrant, densely populated, ecologically sensitive region, effectively mitigating weather-related risks to regional development and ecological preservation.

**Acknowledgements.** This work was jointly supported by Foundation of China Meteorological Administration Aerosol-Cloud and Precipitation Key Laboratory (Grant No. KDW2405), Foundation of Key Laboratory for Cloud Physics and Weather Modification of China Meteorological Administration (Grant No. 2017Z01608) and Foundation of Jiangsu Meteorological Bureau, China (Grant No. KM201803, KQ202513).

## REFERENCES

[1] Chen, H. N., Chandrasekar, V. (2015): The quantitative precipitation estimation system for Dallas-Fort Worth (DFW) urban remote sensing network. – Journal of Hydrology 531: 259-271.
[2] Chen, X. J., Hua, J. J., Pei, Y. J., Wang, Z. C., Liu, S., Liu, S. J., Wang, F. X. (2024): S-band and X-band Radar Observation Characteristics of EF2 Tornado at Qingyuan of Baoding in 2021. – Journal of Applied Meteorological Science 35(5): 564-576.
[3] Cifelli, R., Chandrasekar, V., Chen, H. N., Johnson, L. E. (2018): High resolution radar quantitative precipitation estimation in the San Francisco Bay Area: rainfall monitoring for the urban environment. – Journal of Meteorological Society of Japan 96A: 141-155.
[4] Hartmann, D. L., Tank, A. M. K., Rusticucci, M., Alexander, L. V., Brönnimann, S., Charabi, Y. A. R., Dentener, F. J., Dlugokencky, E. J., Easterling, D. R., Kaplan, A. (2013): Observations: atmosphere and surface, climate change 2013 the physical science basis: working group I contribution to the fifth assessment report of the intergovernmental panel on climate change. – Cambridge University Press, London.
[5] Li, X. M., Zhou, Y. J., Xiao, H., Wu, W., Zhai, L. (2017): Research on the evolution characteristics of hygrometeors in a thunderstrom cell with X-band dual-polarimetric radar. – Chinese Journal of Atmospheric Sciences 41(6): 1246-1263.
[6] Li, C. E., Wu, M. F., Hu, W., Zhang, Y. T., Zhao, X. (2020): Analysis of the Characteristics of X-band dual-polarization radar during a hail weather in spring. – Journal of Anhui Agriculture Science 48(15): 230-233.
[7] Ma, J. L., Su, D. B., Jin, Y. L., Li, R. J. (2012): The impact of attenuation of X-Band dual linear polarimetric radar on hail recognition. – Plateau Meteorology 31(3): 825-835.
[8] Ma, S. Q., Chen, H. B., Wang, G. R., Zhen, X. Q., Xu, X. P., Li, S. T. (2019): Design and initial implementation of array weather radar. – Journal of Applied Meteorological Science 30(1): 1-12.
[9] Nguyen, P., Thorstensen, A., Sorooshian, S., Hsu, K., Aghakouchak, A., Ashouri, H., Tran, H., Braithwaite, D. (2018): Global precipitation trends across spatial scales using satellite observations. – Bulletin of the American Meteorological Society 99(4): 689-697.
[10] Papalexiou, S. M., Montanari, A. (2019): Global and regional increase of precipitation extremes under global warming. – Water Resources Research 55(6): 4901-4914.

[11] Song, G., Lei, L., Ma, J. L., Ma, J. L. (2022): Characteristic and application of X-band dual-polarization radar in severe convection weather in Beijing. – Mid-low Latitude Mountain Meteology 46(6): 63-69.
[12] Su, Y. Y., Liu, L. P. (2022): Comparison of mesocyclone identification results between S-band dual polarization radar and X-band phased array weather radar. – Meteorological Monthly 48(2): 229-244.
[13] Sun, Q. H., Zhang, X. B., Zwiers, F., Westra, S., Alexander, L. V. (2021): A global, continental, and regional analysis of changes in extreme precipitation. – Journal of Climate 34(1): 243-258.
[14] Takahashi, H. G., Fujinami, H. (2021): Recent decadal enhancement of Meiyu–Baiu heavy rainfall over East Asia. – Scientific Reports 11(1): 13665.
[15] Tian, C. C., Zhang, Y., Zeng, L., Li, H. W., Fu, P. L. (2021): Comparative analysis of the X-band phased array radar and the S-band radar. – Guangdong Meteorology 43(3): 55-59.
[16] Wang, S. P., Mai, W. Q., Yan, L. J., Lin, X. X. (2017): Analysis of X-band dual polarization Doppler weather radar echo of a hailstorm in Guangdong. – Meteorological Monthly 39(2): 12-16.
[17] Wu, C., Liu, L. P., Wang, X. D., Fan, H., Liu, Q. (2014): The measurement influence of reflectivity factor caused by scanning mode from phased array radar. – Journal of Applied Meteorological Science 25(4): 406-414.
[18] Zhang, X., Li, W., Zhang, S. M., Peng, L., Wang, L. Y. (2018): Application of X-band dual-polarization weather radar in hail identification. – Agriculture and Technology 38(11): 134-135.
[19] Zhang, Z., Qi, Y. C., Zhu, Z. W., Li, D. H., Zeng, Q. F., Lan, H. P. (2021): Application of radar quantitative precipitation estimation using S-band and X-band polarimetric radars in Shenzhen. – Acta Meteorologica Sinica 79(5): 786-803.
[20] Zhang, Y. Q., Zhang, W., Zheng, H., Xun, A. P., Li, F. (2023): Application Analysis of S-POL-XPAR Joint Observation in Local Short-time Heavy Precipitation Processes in Xiamen. – Meteorological and Environmental Sciences 46(4): 85-94.
[21] Zhao, J. P., Zhang, Z. C., Zhou, F. Y., Feng, X. W., Li, R. Q., Liu, J. L. (2025): Evaluation and analysis of quantitative precipitation estimation using S-band and X-band radars during typhoon Gaemi affecting Zhejiang. – Journal of Marine Meteorology 45(1): 12-22.
[22] Zhi, J. L., Bai, L. Q., Huang, X. X., Cai, K. L., Zhang, J. J., Li, Z. M., Zhao, M., Huang, S. T. (2024): Observation of the 19 June 2022 Tornado by X-Band Polarimetric Phased Array Radar in Foshan, Guangdong. – Journal of Tropical Meteorology 40(2): 297-312.
[23] Zhuang, X. R., Wang, H., Meng, Q. C., Du, C. Y., Han, X. (2023): Observation and analysis of a mudslide event in Beijing by X-band dualpolarization radar. – Journal of the Meteorological Sciences 43(5): 578-588.


http://www.aloki.hu ● ISSN 1589 1623 (Print) ● ISSN 1785 0037 (Online)
DOI: http://dx.doi.org/10.15666/aeer/2304_71997219